ACS NANO

www.acsnano.org

ARTICLE

Spin Filtering in Epitaxial Spinel Films with Nanoscale Phase Separation

Peng Li,[#,†] Chuan Xia,[#,†] Jun Li,[†] Zhiyong Zhu,[‡] Yan Wen,[†] Qiang Zhang,[†] Junwei Zhang,[†] Yong Peng,[§] Husam N. Alshareef,[*,†] and Xixiang Zhang[*,†]

[†]Physical Science and Engineering Division (PSE), King Abdullah University of Science and Technology (KAUST), Thuwal 23955-6900, Saudi Arabia

[‡]KAUST Supercomputing Laboratory (KSL), King Abdullah University of Science and Technology (KAUST), Thuwal 23955-6900, Saudi Arabia

[§]Key Laboratory of Magnetism and Magnetic Materials of Ministry of Education, School of Physical Science and Technology, Lanzhou University, Lanzhou 730000, Gansu, PR China

S *Supporting Information*

ABSTRACT: **The coexistence of ferromagnetic metallic phase and antiferromagnetic insulating phase in nanoscaled inhomogeneous perovskite oxides accounts for the colossal magnetoresistance. Although the model of spin-polarized electron transport across antiphase boundaries has been commonly employed to account for large magnetoresistance (MR) in ferrites, the magnetic anomalies, the two magnetic phases and enhanced molecular moment, are still unresolved. We observed a sizable MR in epitaxial spinel films ($NiCo_2O_{4-\delta}$) that is much larger than that commonly observed in spinel ferrites. Detailed analysis reveals that this MR can be attributed to phase separation, in which the perfect ferrimagnetic metallic phase and ferrimagnetic insulating phase coexist. The magnetic insulating phase plays an important role in spin filtering in these phase separated spinel oxides, leading to a sizable MR effect. A spin filtering model based on Zeeman effect and direct tunneling is developed to account for MR of the phase separated films.**

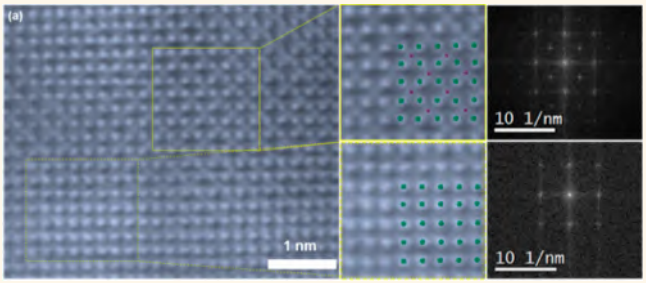

KEYWORDS: *magnetoresistance, phase separation, spinel, spin filter, direct tunneling, Zeeman effect*

Since the discovery of giant magnetoresistance (GMR) in Fe−Cr−Fe superlattice,[1,2] spin-dependent magnetoresistance has been at the heart of spintronics. Accompanied by the discovery of GMR in metallic inhomogeneous systems,[3] tunneling magnetoresistance was found in metallic ferromagnet-insulator systems.[4] The key to this magnetoresistance (MR) is the spin-dependent scattering that occurs in inhomogeneous systems, *e.g.*, superlattice or granular systems. Epitaxial perovskite oxide thin films, such as $La_{1-x}Sr_x(Ca)MnO_3$, also show colossal magnetoresistance (CMR) near the Curie temperature,[5,6] which can be ascribed to the shift in Curie temperature under a magnetic field, where the ferromagnetic-metallic state is governed by a double exchange interaction. In some Manganite, much larger MR has been attributed to the collapse of the charge-ordered insulating state in the submicrometer-scale phase separation between the ferromagnetic metal and the charge-ordered states.[7] So far, phase separation-induced GMR has only been observed within perovskite systems.

In contrast to the CMR observed in epitaxial perovskite films, a moderate, negative MR (about −10% to −20% at 9 T) was observed in epitaxial spinel ferrite films (*i.e.*, Fe_3O_4, $ZnFe_2O_4$, $Co_xFe_{3-x}O_4$).[8−10] This spin-dependent MR has often been ascribed to domain wall scattering,[8] in which the domain walls are caused by the atomically sharp sublattice (cation) dislocation, or antiphase boundaries (APBs).[11,12] Although the spin chain model based on APBs can account for modest MR and some magnetic properties observed in epitaxial Fe_3O_4 films, this model does not adequately explain some other magnetic anomalies in doped Fe_3O_4 (XFe_2O_4) films, *e.g.*, two magnetic phases and enhanced magnetization.[13−15]

Compared to iron-based spinel (XFe_2O_4), cobalt-based spinel (XCo_2O_4) is less often studied for its magneto-transport properties as they apply to spintronics.[16−18] The electrical transport properties and magnetoresistance of epitaxial $NiCo_2O_4$ films grown on (001)-oriented $MgAl_2O_4$ at different substrate temperatures have only recently[16,18] been investigated for applications such as energy storage,[19−21] electrocatalytic

Received: March 13, 2017
Accepted: May 1, 2017
Published: May 8, 2017

DOI: 10.1021/acsnano.7b01743
ACS Nano 2017, 11, 5011−5019

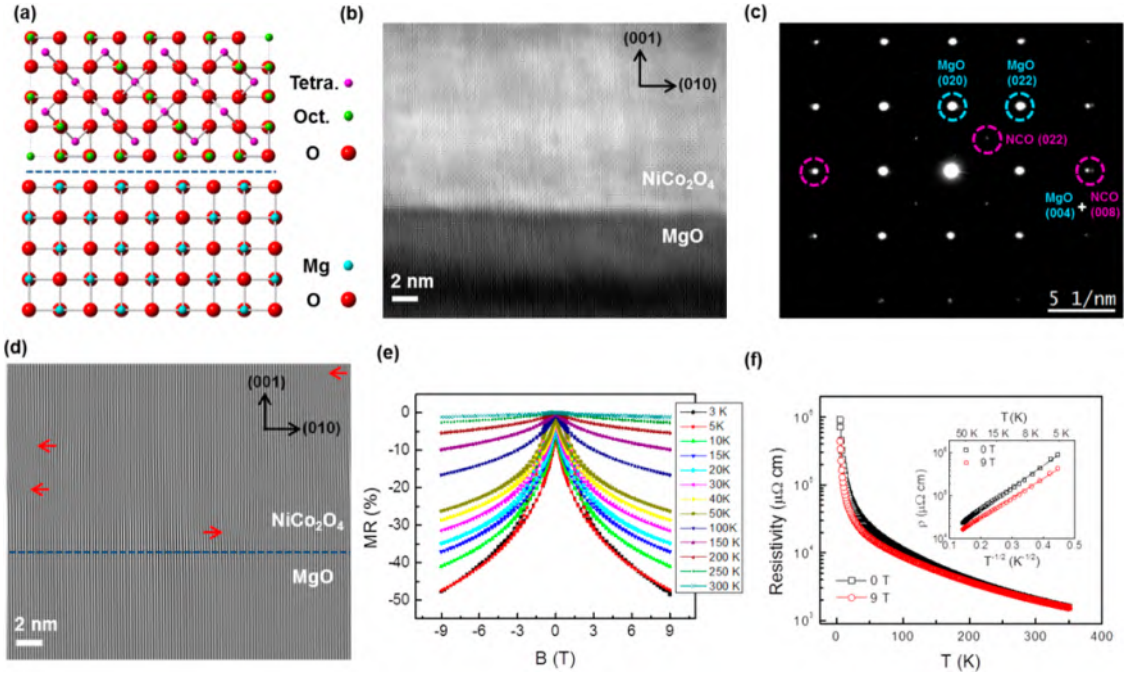

Figure 1. (a) The schematic drawing of the cross-section of (001)-oriented $NiCo_2O_4$ crystal structure on (001)-oriented MgO substrate in the ideal case. The red balls represent oxygen atoms, the blue balls represent Mg atoms, the green balls indicate the octahedral sites (B-sites (occupied evenly by Ni and Co atoms), and the purple balls represent tetrahedral sites (A-sites) (occupied by Co atoms). (b) Atomic-scale HAADF image of the epitaxial growth of $NiCo_2O_4$ (001) on MgO (001) substrate (Sample 1). (c) Selected area diffraction pattern including both $NiCo_2O_4$ film and MgO with an aperture of 40 nm, revealing the cube-on-cube orientation relationship. (d) The filtered image of (b) using a pair of (020) reflections. The lattice mismatch dislocations in $NiCo_2O_4$ are indicated by arrows. (e) In-plane magnetic field-dependent MR of epitaxial $NiCo_2O_4$ film at various temperatures. (f) Temperature dependence of resistivity under different magnetic fields. The inset gives the plot of resistivity of $NiCo_2O_4$ film on $T^{-1/2}$.

activity,[22] and photodetectors.[23,24] However, no sizable MR was observed in these studies over a broad temperature range of 2 to 300 K.[16,18]

However, in cobalt-based epitaxial spinel $NiCo_2O_4$ thin films grown on MgO substrates, we observed a giant magnetoresistance (GMR) of −50% at 9 T and 2 K, which is much larger than the magnetoresistance (MR) observed in iron-based spinel Fe_3O_4thin films. To understand this larger MR, we performed magnetic characterization and high resolution transmission electron microscopy (TEM) experiments on the epitaxial spinel $NiCo_2O_4$ films. We found that these films are composed of two phases: a ferrimagnetic conducting phase (normal $NiCo_2O_4$) and a ferrimagnetic insulating phase ($NiCoO_{4-\delta}$). We demonstrated that the observed GMR can be ascribed to the spin-filtering effect in this phase-separated material, rather than the APB model often employed to interpret MR observed in Fe_3O_4.

RESULTS AND DISCUSSION

In this study, two 18 nm thick, epitaxial $NiCo_2O_4$ films were grown on (001) MgO single-crystal substrates using pulsed laser deposition under an O_2 pressure of 50 (Sample 1) and 0 mTorr (Sample 2) respectively (see Methods). Shown in Figure S1 is the XRD pattern collected on Sample 1. In θ-2θ pattern, only a relatively weak peak of $NiCo_2O_4$ (004) diffraction is observed at 44.6°, close to the strong (002) peak of MgO diffraction at 42.9°, which indicates that the $NiCo_2O_4$ thin film was epitaxially grown along (001) orientation on the (001) MgO substrate. The ideal $NiCo_2O_4$ crystal has an inverse spinel structure and a face-centered cubic oxygen sublattice, where nickel cations occupy the octahedral sites (B-sites) while cobalt cations are evenly distributed between both the octahedral (B-sites) and the tetrahedral sites (A-sites). Considering the lattice constants of $NiCo_2O_4$ (8.11 Å) and MgO (4.20 Å), a small anionic sublattice mismatch of −3.4% should facilitate the epitaxy of $NiCo_2O_4$ (001) on MgO (001), as shown in Figure 1a. To further confirm this relationship, cross sections of $NiCo_2O_4$/MgO from Sample 1 were imaged. The spherical-aberration corrected high-angle annular dark-field (HAADF) image of the interface (Figure 1b) clearly shows good epitaxy of $NiCo_2O_4$ film on MgO (001) substrates. The corresponding selected-area electron diffraction (SAED) pattern (Figure 1c) exhibits the characteristics of a face-centered cubic crystal and further confirms good epitaxy growth. The diffraction spots of $NiCo_2O_4$ (purple dashed circle) are much weaker than those of the MgO substrates (blue dashed circle) because the $NiCo_2O_4$ film is ultrathin at 18 nm. As the Miller index number increases, the separation of the spots in both materials become more apparent due to their lattice mismatch. We filtered the Fast Fourier Transformation (FFT) image from Figure 1b and obtained the inverse FFT image by using a pair of diffraction spots MgO(002)/$NiCo_2O_4$(004). Several dislocations of cations were clearly observed, indicated by arrows in Figure 1d, which originated from the lattice mismatch (−3.4%) between $NiCo_2O_4$ and MgO. We therefore demonstrated the epitaxial growth of $NiCo_2O_4$ films on MgO(001) substrates.

The magnetoresistance measured at different temperatures on Sample 1 is shown in Figure 1e. Unexpectedly, a large, negative MR, as large as −50% at 9 T, was observed at 2 K, which is in sharp contrast to the very small or nonexistent MR effect in $NiCo_2O_4$ grown on $MgAl_2O_4$ substrates.[16,18] It is clear

DOI: 10.1021/acsnano.7b01743
ACS Nano 2017, 11, 5011−5019

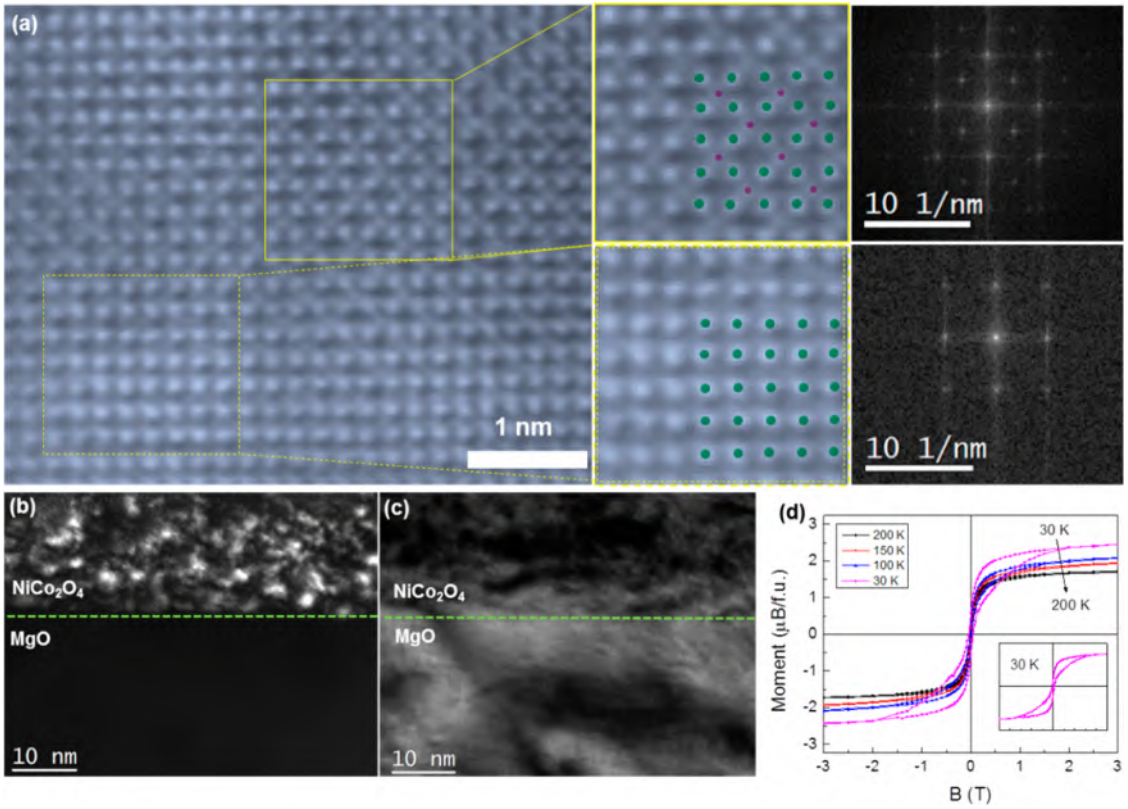

Figure 2. (a) High resolution HAADF-STEM image of epitaxial $NiCo_2O_4$ (001) film. The solid yellow square region is representative of the ideal spinel $NiCo_2O_4$ crystal, magnified to the right with green (B-sites) and purple (A-sites) dots added for clarity. The dashed yellow square region shows an imperfect $NiCoO_{4-\delta}$ crystal in which the cations at A-sites are missing, magnified to the right with green dots added for clarity. The solid yellow square region gives an ideal $NiCo_2O_4$ crystal. The corresponding FFT diffraction images are shown in the far right panel. The absence of diffraction spots of (022) in the diffraction pattern for the dashed square region confirms the imperfection of the spinel crystal. (b) The dark-field (002) TEM image taken with (022) reflection. The dark-field image shows the distribution of ideal spinel and imperfect spinel $NiCo_2O_4$ crystals in the film, which presents characteristics of a granular material. (c) Corresponding bright-field image. (d) Magnetic hysteresis loops of epitaxial $NiCo_2O_4$ film at various temperatures. The inset shows the hysteresis at 30 K for clarity. The behavior of the low temperature hysteresis can be ascribed to the coexistence of two magnetic phases in the material.

that MR strongly depends on temperature (also see Figure S2, MR−T curve, where MR decreases from −50% at 2 K to −1.1% at 300 K), a typical feature of a spin-dependent MR.[4,25] To explore the physics behind the observed large MR, the dependencies of resistivity on temperature and magnetic field were measured in the temperature range from 2 to 300 K with a magnetic field up to 9 T, in which the magnetic field was applied along [100] direction in the $NiCo_2O_4$ film plane. The temperature dependent resistivity under zero and 9 T is shown in Figure 1f. Both resistivity curves show nonmetallic behavior, *i.e.*, resistivity increases monotonically with decreasing temperature. As expected, the high field resistivity is lower than the resistivity under zero field, over the whole temperature range due to the spin-dependent MR effect, in good agreement with data shown in Figure 1e (the field-dependent MR). Although the room temperature resistivity of the $NiCo_2O_4$ film, $\sim 3 \times 10^3$ $\mu\Omega$·cm, is consistent with the room temperature resistivity observed on $NiCo_2O_4/MgAl_2O_4$,[16,18] no metal−insulator transition was observed in our sample.

To gain a deeper understanding of the electrical transport mechanism, we carefully analyzed the temperature dependence of resistivity of epitaxial film (Sample 1) under different magnetic fields (shown in Figure 1f) and found that the low temperature data can be well described by $\rho(T) \propto \exp(C/T^{1/2})$.[26] This temperature dependence of $R(T)$ describes the electrical transport driven by the tunneling effect in metallic-insulator granular materials.[26] Therefore, further study into the structure and composition of the epitaxial film is essential to understanding the origin of the spin-dependent tunneling transport.

By analyzing the atomic-scale HAADF image of $NiCo_2O_4$ (Figure 2a), we found that the film is inhomogeneous even within an area as small as 5 nm. By magnifying and comparing the images of sublattice in the dashed and solid yellow squares, we find an interstitial atom occupying both tetrahedral sites (A-sites) and the octahedral sites (B-sites) in the solid square, whereas this interstitial atom is absent from the A-sites in the dashed square (Figure 2a). To clearly illustrate the difference between the two regions, we use purple and green dots overlapping on the A- and B-sites in the amplified images (Figure 2a). In addition, we performed FFT of the images to further demonstrate the structural difference between the two regions. The difference in the FFT diffraction patterns is evident: four diffraction spots in the solid square are missing from the dashed square. Actually, the FFT diffraction pattern in the upper panel is the (022) diffraction pattern of the spinel. Comparing the TEM images of the solid square in Figure 2a with the schematic atomic occupation in Figure 1a indicates that the crystal in the solid square has the standard inverse spinel structure. Apparently, the structure of the crystal in the

DOI: 10.1021/acsnano.7b01743
ACS Nano 2017, 11, 5011−5019

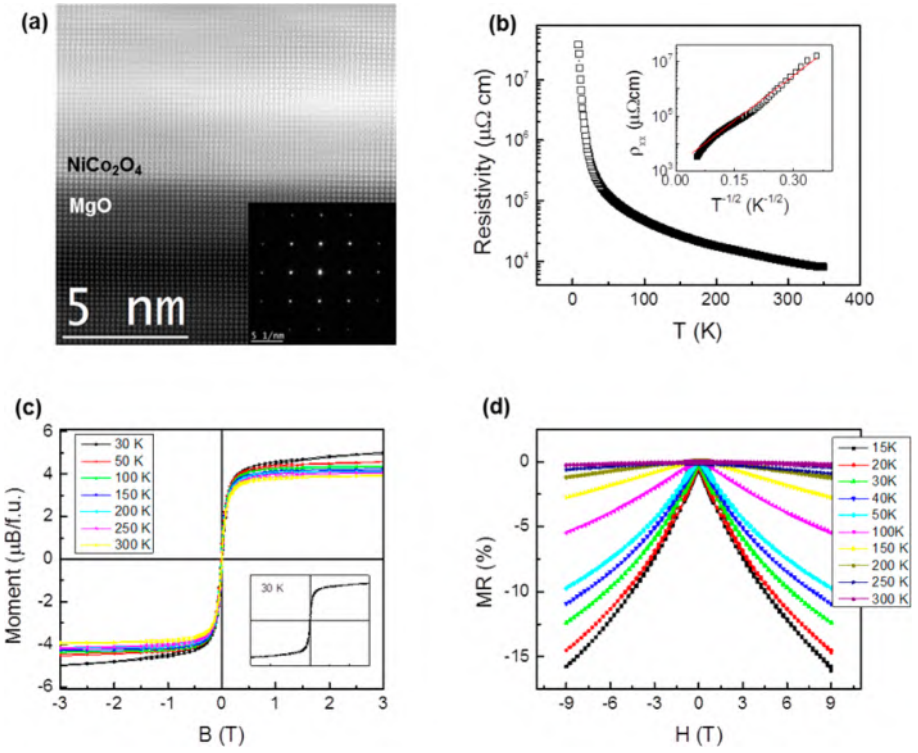

Figure 3. (a) High resolution HAADF-STEM image of epitaxial $NiCo_2O_4$(001) film (Sample 2) fabricated under zero oxygen partial pressure. (b) The temperature dependence of resistivity of $NiCoO_{4-\delta}$ film (Sample 2), and the inset shows a nearly linear dependence of $\ln \rho_{xx}$ on $T^{-1/2}$. (c) Magnetic hysteresis loops of epitaxial $NiCo_2O_4$ film (Sample 2) at various temperatures. The behavior of these loops is representative of a single magnetic−phase material. (d) In-plane magnetic field-dependent MR of epitaxial $NiCo_2O_4$ film (Sample 2) obtained at various temperatures.

dashed square (Figure 2a) significantly deviates from the ideal spinel structure, based on the HAADF images and their FFT patterns. Another feature worth noting in the solid square is the dimness of the A-sites; the atomic column formed only by Co ions (A-sites) is weaker than that of the column formed by both Co and Ni ions (B-sites). This can be ascribed to the difference in the effective Z contrast ($Z_{Co} < Z_{Ni-Co} < Z_{Ni}$) in ideal inverse spinel $[Co_A(NiCo)_BO_4]$ as confirmed by neutron diffraction.[27] On the basis of the above experimental results and analysis, we conclude that Sample 1, as a composite or granular material, is composed of two phases (ideal spinel in the solid square and imperfect spinel in the dashed square).

In order to find the distribution of the two phases and their relative volume fractions in this $NiCo_2O_4$ film, we imaged the materials in dark-field mode using the (220) reflection of the ideal spinel structure under a two-beam condition, as shown in Figure 2b. The corresponding bright-field TEM image is shown Figure 2c. In the dark-field image, the MgO substrate is dark because it does not contribute to the (220) reflections of the spinel. The bright areas in Figure 2b are the ideal spinel crystals from the solid square in Figure 2a; whereas the dark areas in Figure 2b are the imperfect spinel crystals from the dashed square in Figure 2a. The dark-field images confirm again the phase separation in Sample 1. Hereafter, we designate the ideal-spinel phase as Phase I, and the imperfect-spinel phase with A-site vacancies as Phase II. By using a simple simulation of the dark-field image in Figure 2b, we estimate that the ratio of dark region with cationic vacancies (Phase II) to total film is about 20 ± 5%.

Since the magnetic properties of the spinel, *e.g.*, the saturation magnetization and coercive field, are determined by the distribution of cations, magnetic characterization should be a very powerful tool to detect the different phases. We measured the magnetic hysteresis loops of the film at different temperatures. A single-phase, crystalline $NiCo_2O_4$, $(Co^{3+})_A[Ni^{2+}Co^{3+}]_BO_4$,[27] is a ferrimagnet in which magnetic moments on A-sites and B-sites are coupled antiferromagnetically, and which exhibits a net molecular moment of 2 μB with Co^{3+} (4 μB) and Ni^{2+} (2 μB). To correctly obtain the magnetic properties of the $NiCo_2O_4$ films, we had to subtract the contribution of the MgO substrates from the experimental data (Figure S3). We could only obtain reliable magnetic data above 30 K because of the strong paramagnetic contribution of MgO at low temperatures. Shown in Figure 2d are the representative hysteresis loops obtained at different temperatures (see more hysteresis in Figure S4). For clarity, the loop obtained at 30 K is replotted in the inset of Figure 2d. The behavior of the 30 K loop with a total moment of 2.58 μB/f.u. shows two distinct magnetic phases with different saturation magnetization and coercive field properties. A close inspection reveals that all of the hysteresis loops obtained in the temperature range of 30 to 150 K exhibit two magnetic phases (Figure S4). The higher coercive field feature decreases faster with increasing temperature, and so above 150 K the separation between the two phases fades.

The abnormal magnetic properties, *e.g.*, coexistence of two magnetic phases[14,18,28] and enhanced magnetization,[9,13,15] have been frequently observed in oxides with spinel structure. Although two magnetic phases were observed in several studies on epitaxial $CoFe_2O_4$ and $NiCo_2O_4$ films,[14,18,28] a full definition of the two phases has not been achieved. The enhanced magnetic moments in $NiFe_2O_4$,[13] Fe_3O_4,[15] and even in

DOI: 10.1021/acsnano.7b01743
ACS Nano 2017, 11, 5011−5019

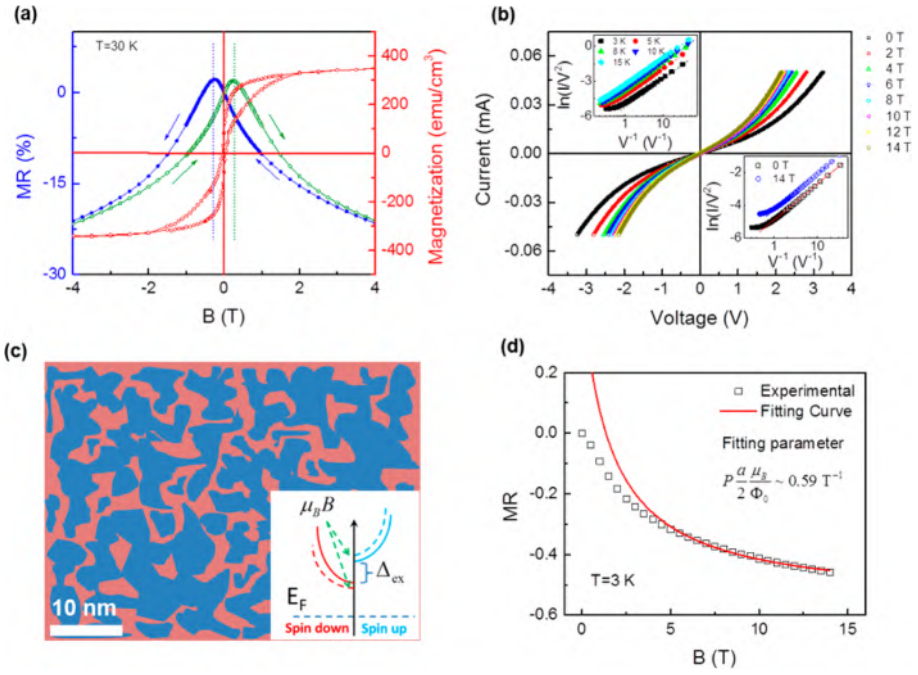

Figure 4. (a) The correlation between the behavior of MR and magnetization as a function of the applied magnetic field obtained at 30 K on Sample 1. The fields at which maximum resistivity appears are much larger than the coercive fields of the magnetic hysteresis loop. Close analysis reveals that these fields correspond to the coercive field of the hard phase (ideal spinel $NiCo_2O_4$). The arrows indicate the scan direction of the magnetic field. (b) Nonlinear $I-V$ curves of the $NiCo_2O_4$ film (Sample 1) obtained at 3 K and various magnetic fields. The upper inset shows the linear dependence of ln J/V^2 on ln $1/V$ at B = 0 and different temperatures. The bottom inset presents the linear dependence of ln J/V^2 on ln $1/V$ obtained at 3 K and with different magnetic fields.(c) The schematic representation of the granular-like distribution of the two phases in Sample 1. The blue regions and orange regions respectively represent Phase I (ideal spinel $NiCo_2O_4$) and Phase II (imperfect $NiCoO_{4-\delta}$ with cationic vacancies at A-sites). The inset shows the schematic drawing of the conduction band splitting due to the exchange splitting in Phase II and the Zeeman effect. After application of the magnetic field, the bottom of conduction bands shift from the solid lines to the dashed lines for spin-up (blue) and spin-down (red) electron tunneling, due to the Zeeman effect. (d) Magnetic field-dependent MR ratio obtained at 3 K with a fixed voltage bias (Sample 1). The red curve is the fitted data at the high magnetic field region using the spin-filtering model.

antiferromagnetic $ZnFe_2O_4$,[9] were suggested to stem from cationic inversion. Note that the saturation magnetization of Sample 1 at 30 K is 2.58 μB/f.u. and significantly larger than the 2 μB/f.u. at zero K.[27]Therefore, the magnetic results strongly support that the thin film is composed of two phases, and that one phase has a much larger saturation magnetization than the ideal $NiCo_2O_4$.

Now let us discuss Phase II. On the basis of the TEM images, we already know that the atoms at A-sites are missing. Two possibilities for these missing cations are a) all cations are distributed in B-sites or b) cations at A-sites are missing and the number of cations at B-sites remains unchanged. We calculated the energy of the two situations numerically (Note 1 in SI), and found that the latter possibility (b) is energetically more likely. In this case, the moments of Co^{3+} (4 μB) and Ni^{2+} (2 μB) are ferromagnetically coupled and lead to a total moment 6 μB/f.u. By taking 2.58 μB as the total moments and using $2(1-x)+6x = 2.58$ (Note 1 in SI), we found the volume fraction of Phase II $x \approx 15\%$. One should note that the value x obtained here is underestimated, because we assume that M_s = 2.58 μB at 30 K and M_s = 2 μB at 0 K for Phase I. Therefore, the value x = 15% obtained from the magnetic data is in consistent with the value $x = 20 \pm 5\%$ obtained using the TEM images. Moreover, we found that x = 19% when using the extrapolated saturation magnetization M_s = 2.78 μB at 0 K (Figure S5), which is even closer to the value x obtained from the TEM images.

The next questions to be answered are which phase is more electrically conducting, and how does phase separation affect the transport and magnetic properties of the film? And so, we studied an epitaxial $NiCo_2O_4$ film deposited without filling oxygen (vacuum conditions of 0 mTorr), keeping the other conditions unchanged (Sample 2). The structure of Sample 2 was then studied using HAADF, as shown in Figure 3a. Interestingly, we can hardly find any A-site atoms in this HAADF image, indicating that the A-site atoms are nearly excluded through charge balance caused by oxygen vacancies. Consequently, it is difficult to observe (022) diffraction spots of the spinel from the SAED pattern, as shown in the inset of Figure 3a. On the basis of the TEM experiments, we know that Sample 2 is mainly composed of Phase II. Because both samples are deposited under different environments, we are motivated to investigate their valence states. The X-ray photoelectron spectra of Samples 1 and 2 demonstrates that Ni^{2+} and Co^{3+} are dominant in both samples and that Co^{2+} and Co^{3+} coexist on B sites in both samples due to the presence of Ni^{3+} on B sites (Figure S6). Nevertheless, the cationic valence inversion between Ni and Co on B sites (Ni^{2+}(2 μB) Co^{3+}(4 μB) or Ni^{3+}(3 μB) Co^{2+}(3 μB)) will not affect the net molecular moment of 2 μB/f.u. (Phase I) and 6 μB/f.u. (Phase II). Therefore, it is interesting to study the transport and magnetic properties of Sample 2, and then compare those with the properties of Sample 1. Shown in Figure 3b is the temperature dependence of resistivity of Sample 2 under zero

DOI: 10.1021/acsnano.7b01743
ACS Nano 2017, 11, 5011−5019

magnetic field. By comparing the results in Figure 3b to those in Figure 1f, we found that the low temperature resistivity of Sample 2 is about 2 orders of magnitude higher than that of Sample 1, though the room temperature resistivity of the two samples is almost identical. The much stronger temperature dependence in Sample 2 can be clearly seen from the normalized resistivity data, $\rho(T)/\rho(350\ \mathrm{K})$, in Figure S7. From the resistivity data, we also confirm that Phase II is much less conducting than Phase I. By fitting the data to the tunneling conduction model (inset of Figure 3b), we found that the resistivity of Sample 2 can be roughly described by tunneling conduction over the whole temperature range (15−350 K).[26] The fitted average charging energy for Sample 2 (C = 1.46 meV) is much larger than that for Sample 1 (C = 0.56 meV). Nonetheless, the imperfect linearity of the $\ln \rho \propto T^{-1/2}$ curve at low temperatures implies a much more complicated conduction mechanism in Sample 2 than in Sample 1. Shown in Figure 3c is the magnetic field dependence of magnetization ($M(H)$) at different temperatures. The saturation magnetization at a low temperature (30 K) for Sample 2 is 5.34 μB/f.u. (7 T), much larger than that in Sample 1. Another very important feature in the 30 K $M(H)$ curve (inset) is that the hysteresis loop is very similar to a simple, regular hysteresis loop commonly observed on a single-phase, ferrimagnetic material. Much smaller coercive fields are observed in comparison with those observed in Sample 1 at corresponding temperatures. It is clear that Phase II is magnetically a much softer ferrimagnetic phase with much higher saturation magnetization in comparison with Phase I.

Using the saturation magnetization, M_s(30 K) = 5.34 μB/f.u., we found the volume fraction x of Phase II in Sample 2 is 83.5% (see Note 1 in SI). Using the extrapolated value (Figure.S5), M_s(0 K) = 5.48 μB/f.u. we obtained x = 87%. These volume fraction estimates obtained from magnetic measurements agrees with x = 90% ± 5%, obtained from the element analysis (Note 1 in SI). Due to the very large volume fraction of Phase II in Sample 2, it is very difficult to find the ideal spinel $NiCo_2O_4$ nanocrystals in the TEM images (Figure 3a) and (220) diffraction in SAED pattern (inset of Figure 3a). Since Sample 2 is much more insulating than Sample 1, we come to the conclusion that Phase II is a much more insulating, magnetically softer ferrimagnetic phase with much higher saturation magnetization than Phase I (the ideal spinel $NiCo_2O_4$) over the whole temperature range. (Figure S8 shows the temperature dependence of H_c and M_s for both samples).

To further confirm that the metallic Phase I in Sample 1 is consistent with metallic spinel $NiCo_2O_4$ previously reported by others groups,[16,18,29] the metallic $NiCo_2O_4$ film was prepared under 250 mTor O_2 atmosphere. It is found that this $NiCo_2O_4$ film showed a metallic type of electrical conduction, a negligibly small MR ratio, a molecular moment near 2 μB/f.u. and a hysteresis loop of single phase with high coercive field up to 2 kOe at low temperatures (Figure S9). All these properties are quite similar to those of Phase I in Sample 1.

Similarly, we have measured the magnetoresistance in Sample 2, as shown in in Figure 3d. Apparently, MR in Sample 2 depends strongly on temperature as well, but the size is much smaller than that in Sample 1. The MR in Sample 2 is similar to that observed in other spinel materials.[8−10] The plot shown in Figure S2 is a comparison of the MR−T curve obtained for both samples. The difference in MR ratio of the two samples will be discussed below.

To better understand the GMR in phase-separated $NiCo_2O_4$ epitaxial films, we compare the magnetic field-dependence of MR and magnetization in same plot. Shown in Figure 4a is the in-plane MR and the in-plane magnetization of Sample 1 measured at 30 K. There are several features in Figure 4a that are strikingly different from those observed previously in different granular materials, such as ferromagnetic transition metal/noble metals[30,31] and ferromagnetic transition metal/insulator.[4,32]

The first and most interesting feature shown in Figure 4a is that the peak in MR (the most resistive state) does not occur at the coercive field of the magnetic hysteresis loop as observed in common granular materials. Although a similar butterfly shaped behavior in the MR curve is observed as in conventional granular materials, the peak in MR occurs at a much stronger magnetic field. In $NiCo_2O_4$, due to the spin-dependent tunneling across the insulating Phase II with a weaker coercive field,[33,34] the measured coercive field in the magnetic hysteresis loop and the low-field magnetic properties of the sample is dominated by Phase II, which has a higher saturation magnetization and a lower magnetic coercive field than Phase I. On the other hand, we see that the maximum resistivity state and the butterfly shaped low-field MR is governed by Phase I with stronger coercive field, which can be ascribed to the spin dependent tunneling across the insulating phase II with a weaker coercive field.[33,34]

Another feature is that the MR does not exhibit any saturation magnetization behavior up to 9 T over the whole temperature range (Figure 1e) in epitaxial $NiCo_2O_4$ film; this contrasts sharply with conventional granular materials, in which MR saturates quickly at magnetic saturation fields.[4,30−32] This striking difference must originate from the fact that both the insulating phase and the conducting phase are ferrimagnetic in this sample, whereas in the conventional granular materials, only one phase is magnetic. Evidently, the physics behind the MR in $NiCo_2O_4$ is completely different from that in common granular material. Given this unusual characteristic of $NiCo_2O_4$ films, *i.e.*, that the insulating Phase II is also ferrimagnetic, we look to the spin-filtering effect to understand the behavior of MR in this phase-separated magnetic material.[35]

We show that the origin of MR is indeed from the spin-filtering effect by measuring the $I-V$ curves using a four-terminal configuration at different magnetic fields, as shown in Figure 4b. The nonlinear dependence is ascribed to the tunneling mechanism. More importantly, the current increases significantly with increasing magnetic field under the same applied electric potential, suggesting a large negative magnetoresistance (Figure 1e), confirming the observation of GMR with a constant current measurement. Detailed analysis also reveals that the current density of epitaxial $NiCo_2O_4$ films can be described by direct tunneling across a tunnel barrier,[36]

$$J \propto \sqrt{2m^*\Phi}\left(\frac{e}{h}\right)^2 \frac{V}{d} \exp\left[\frac{-4\pi d\sqrt{2m^*\Phi}}{h}\right] \quad (1)$$

where h is the Planck constant, e is the electronic charge, m^* is the effective mass of an electron, Φ is the barrier height, V is the applied bias and d is the barrier thickness. To focus on the behavior of the $I-V$ curves, we can rewrite eq 1 as the following:

$$\ln \frac{J}{V^2} \propto \ln \frac{1}{V} - \frac{4\pi d\sqrt{2m^*\Phi}}{h} \quad (2)$$

DOI: 10.1021/acsnano.7b01743
ACS Nano 2017, 11, 5011−5019

We then plotted the experimental data following eq 2; see the upper inset of Figure 4b. The nearly linear dependence of ln J/V^2 on ln $1/V$ in the curves obtained at various temperatures (B = 0 T) strongly suggests that the electrical transport in the phase-separated $NiCo_2O_4$ films is dominated by direct tunneling. The deviation from the linear dependence at a high electric field in these curves may be ascribed to the mechanism of the electrical transport transforming from direct tunneling under low electric potential, to Fowler-Nordheim tunneling through a triangle-shaped barrier under high electric potential.[37] With an increase of magnetic field (T = 3 K), the absolute value of the intercept of the curves ($\frac{4\pi d\sqrt{2m^*\Phi}}{h}$) is decreasing (bottom inset of Figure 4b), indicating asignificant reduction of the tunneling-barrier height.

To understand the behavior of MR at high magnetic fields, we employed the two-current model, in which the spin-up and spin-down electrons tunnel through different barriers caused by exchangesplitting and field-dependent Zeeman energy. A schematic diagram of the granular-like percolation system in Sample 1 and the band structure under different magnetic fields are shown in Figure 4c and its inset, respectively. The tunneling barrier in eqs 1 and 2 can be described as $\Phi_{\uparrow(\downarrow)} = \Phi_0 + (-)\Delta/2 + (-)\mu_B B$,[38] in which Φ_0 is the average tunneling-barrier height, Δ represents the exchange splitting of the conduction band bottom and $\mu_B B$ is the Zeeman energy under magnetic fields (dashed lines in Figure 4c). Note that the Zeeman energy (on the order of $10^{-1} \sim 10^{-2}$ meV) can be considered as a perturbation to Φ_0 (on the order of 10^{0} eV) and Δ (on the order of 10^{-1} eV). It is evident that the tunneling current will vary with the applied magnetic field B, a correlation that we can call the MR effect.

On the basis of the two-current model and the Zeeman effect on spin filtering, we can obtain the ratio of the tunneling-current density in the B field to that of the zero magnetic field,

$$\frac{J(B)}{J(0)} = 1 + P\frac{a}{2}\frac{\mu_B B}{\Phi_0} \tag{3}$$

where P is the tunneling-spin polarization, and $a = \frac{-4\pi d\sqrt{2m^*\Phi}}{h}$ (see more detailed derivation in Note 2 in SI). Therefore, the dependence of MR on magnetic field B can be calculated as

$$\begin{aligned} \mathrm{MR} &= \frac{R(B) - R(0)}{R(0)} \\ &= \frac{V/I(B) - V/I(0)}{V/I(0)} \\ &= \frac{1}{1 + P\frac{a}{2}\frac{\mu_B B}{\Phi_0}} - 1 \end{aligned} \tag{4}$$

It is clear that this is a hyperbolic function on the magnetic field. We then fit the field-dependent MR data, extracted from the $I-V$ curves of Sample 1 at 3 K, and fixed the voltage (2 V) to eq 4. As shown in Figure 4d, the behavior of MR in the high magnetic field region can be described by eq 4 with a fitted parameter $P\frac{a}{2}\frac{\mu_B}{\Phi_0} \sim 0.59\ \mathrm{T}^{-1}$ for $B > 4$ T. The discrepancy between the fitted data and the experimental data in the low field region, particularly for $B < 4$ T, could be explained by the misalignment of the magnetic moments of Phase I influencing the spin-dependent conduction; this is supported by the discrepancy between the field-increase and field-decrease MR curves below 4 T. If we take the average barrier height $\langle\Phi_0\rangle \sim$ 3.5 eV (2 K) obtained from Brinkman–Dynes–Rowell (BDR) fitting of normalized conductance (Figure S10),[39] the calculated parameter of $P\frac{a}{2}\frac{\mu_B}{\Phi_0}$ should be 0.0013 T^{-1}. Owing to the characteristics of granular materials and the random distribution of two phases, the magneto-transport should be a multiple tunneling process with a random distribution of barrier width and barrier height. This could be one origin of the significant discrepancy between the values of the calculated and fitted parameter of $P\frac{a}{2}\frac{\mu_B}{\Phi_0}$. We also fit the field-dependent MR data from Figure 1e to eq 4 (Figure S11a). The fitted parameter $P\frac{a}{2}\frac{\mu_B}{\Phi_0}$ attenuates quickly as temperature increases (Figure S11b). The barrier height decreases slightly as the temperature rises, which is confirmed by the decreasing absolute value of intercept ($\frac{4\pi d\sqrt{2m^*\Phi}}{h}$) (upper inset of Figure 4b). Therefore, the fast drop of $P\frac{a}{2}\frac{\mu_B}{\Phi_0}$ with the temperature should be ascribed to the dramatic decrease of P, indicating that the spin polarization decreases with increasing temperatures, as observed in other experiments based on ferrite materials.[37]

The electrical transport in Sample 1, which was dominated by spin-dependent tunneling, can also be observed in the $R(T)$ curves under different magnetic fields. By fitting the $R(T)$ curves (Figure 1f) to the tunneling-dominated transport in granular materials, $\rho(T) \propto \exp(C/T^{1/2})$, we find the average charging energy C = 0.56 meV for B = 0 and C = 0.49 meV for 9 T. The slightly smaller energy barrier at 9 T indicates that the energy barrier was reduced by the magnetic field. This magnetic field-dependent tunneling barrier can be ascribed to the spin-filtering effect.[35,40,41]

To understand why the MR observed in Sample 2 is smaller than the MR in Sample 1, we measured the $I-V$ curves at low temperatures. The linear $I-V$ curves of Sample 2 at different magnetic fields indicate imperfect direct tunneling and Ohmic-like behavior, as shown in Figure S12. Because the volume fraction of the insulating phase (Phase II) is about 90%, much larger than the percolation threshold for 2D materials,[42] the conduction phase (Phase I) should still be present as conduction inclusions, embedded in the more insulating Phase II (Figure S13). Therefore, the conduction of Sample 2 should be Ohmic-like. Since both Phase I and II are ferrimagnetic, spin-dependent scattering will still play an important role, which leads to a sizable MR in Sample 2. Another feature of Sample 2 is that the behavior of MR in the high magnetic field region shows a more linear than hyperbolic dependence, indicating that the tunneling MR is not a dominant factor. Clearly, the GMR in the phase-separated $NiCo_2O_4$ is successfully understood by our physical model involving the two-current modeland the spin-filtering effect across a ferrimagnetic insulating barrier.

CONCLUSION

In summary, we have observed giant magnetoresistance (GMR) of −50% at 9 T and 3 K in epitaxial spinel $NiCo_2O_4$ films. Structural analysis reveals that the epitaxial spinel $NiCo_2O_4$ film is an inhomogeneous, granular-like system. Phase separation is directly observed by TEM in epitaxial spinel oxides. Phase I, the ideal $NiCo_2O_4$, behaves as a ferrimagnetic conductor, whereas Phase II, the $NiCoO_{4-\delta}$ phase whose Co cations at A-sites are totally missing, behaves as a ferrimagnetic insulator with a very

DOI: 10.1021/acsnano.7b01743
ACS Nano 2017, 11, 5011–5019

high saturation magnetization and a weak coercive field. The butterfly shaped MR at low magnetic fields is related to the moment rotation and spin-dependent scattering of nanoscale ideal spinel $NiCo_2O_4$ crystals (Phase I). The hyperbolic-like MR at high magnetic fields is well understood within the two-current model and the spin-filtering effect across a ferrimagnetic insulating barrier (Phase II). This work provides an alternative perspective and a comprehensive understanding of magnetic anomaly and large negative MR behavior in epitaxial spinel films.

METHODS

The epitaxial $NiCo_2O_4$ films were grown using pulsed laser deposition on (001)-oriented MgO single-crystal substrate at 350 °C under an O_2 pressure of 50 mTorr (Sample 1) and vacuum conditions of 0 mTorr (Sample 2), with a KrF excimer laser (λ = 248 nm) at 10 Hz with a fluence of 2.8 J/cm^2. The metallic sample is prepared under an O_2 pressure of 250 mTorr for comparison. The background vacuum was better than 2×10^{-7} Torr. The growth rate and thickness of the epitaxial $NiCo_2O_4$ films was maintained at 3 Å/min and 18 nm, respectively. The structure was analyzed by X-ray diffraction (XRD, Bruker D8 Discover) with Cu Kα radiation. The samples for transmission electron microscopy (TEM) were prepared by a focused ion beam (FIB) (Helios 450, FEI). The cross sections of the epitaxial $NiCo_2O_4$ films on MgO substrates were imaged using monochromated Cs-corrected high-resolution scanning TEM (Titan 80−300, FEI). Magnetic properties of the epitaxial $NiCo_2O_4$ films were measured using a Quantum Design SQUID magnetometer. Transport properties, including temperature dependent resistivity and magnetoresistance (MR), were measured with a Quantum Design Physical Property Measurement System (PPMS-Dynacool) in the temperature range of 2 to 300 K. The MR in this work is defined as MR = $(R_B - R_0)/R_0$, where R_0 and R_B are the resistance at zero and B magnetic fields, respectively.

To understand the stability of spinel oxides with different compositions and cation distributions, we performed full-potential linearized augmented plane-wave calculations using the WIEN2K package; thus we compared the energy difference between normal spinel $NiCo_2O_4$ and other phases with different cation distributions. The chemical state was confirmed by X-ray photoelectron spectrum (XPS). The element ratio (Ni:Co) was analyzed by electron energy loss spectroscopy (EELS), energy-dispersive X-ray spectroscopy (EDX) and inductively coupled plasma optical emission spectrometry (ICP-OES).

ASSOCIATED CONTENT

Supporting Information

The Supporting Information is available free of charge on the ACS Publications website at DOI: 10.1021/acsnano.7b01743.

XRD of epitaxial films, temperature dependence of normalized resistivity, MR ratio, coercive field and magnetic moment of both samples, XPS of both samples, the metallic conduction behavior of epitaxial $NiCo_2O_4$ sample, $I-V$ curves of sample 2, the detailed elementary analysis, and detailed derivation of spin filtering physical model. (PDF)

AUTHOR INFORMATION

Corresponding Authors

*E-mail: husam.alshareef@kaust.edu.sa.
*E-mail: xixiang.zhang@kaust.edu.sa.

ORCID

Husam N. Alshareef: 0000-0001-5029-2142
Xixiang Zhang: 0000-0002-3478-6414

Author Contributions

#P.L. and C.X. contributed equally.

Notes

The authors declare no competing financial interest.

ACKNOWLEDGMENTS

The research reported in this publication was supported by funding from King Abdullah University of Science and Technology (KAUST). P.L. acknowledges the financial support of CRF-2015-SENSORS-2709 (KAUST) and SABIC postdoctoral fellowship award presented to KAUST.

REFERENCES

(1) Baibich, M. N.; Broto, J. M.; Fert, A.; Vandau, F. N.; Petroff, F.; Eitenne, P.; Creuzet, G.; Friederich, A.; Chazelas, J. Giant Magnetoresistance of (001)Fe/(001) Cr Magnetic Superlattices. *Phys. Rev. Lett.* **1988**, *61*, 2472−2475.

(2) Binasch, G.; Grunberg, P.; Saurenbach, F.; Zinn, W. Enhanced Magnetoresistance in Layered Magnetic-Structures with Antiferromagnetic Interlayer Exchange. *Phys. Rev. B: Condens. Matter Mater. Phys.* **1989**, *39*, 4828−4830.

(3) Berkowitz, A. E.; Mitchell, J. R.; Carey, M. J.; Young, A. P.; Zhang, S.; Spada, F. E.; Parker, F. T.; Hutten, A.; Thomas, G. Giant Magnetoresistance in Heterogeneous Cu-Co Alloys. *Phys. Rev. Lett.* **1992**, *68*, 3745−3748.

(4) Mitani, S.; Takahashi, S.; Takanashi, K.; Yakushiji, K.; Maekawa, S.; Fujimori, H. Enhanced Magnetoresistance in Insulating Granular Systems: Evidence for Higher-Order Tunneling. *Phys. Rev. Lett.* **1998**, *81*, 2799−2802.

(5) Mccormack, M.; Jin, S.; Tiefel, T. H.; Fleming, R. M.; Phillips, J. M.; Ramesh, R. Very Large Magnetoresistance in Perovskite-Like La-Ca-Mn-O Thin-Films. *Appl. Phys. Lett.* **1994**, *64*, 3045−3047.

(6) Jin, S.; Mccormack, M.; Tiefel, T. H.; Ramesh, R. Colossal Magnetoresistance in La-Ca-Mn-O Ferromagnetic Thin-Films. *J. Appl. Phys.* **1994**, *76*, 6929−6933.

(7) Uehara, M.; Mori, S.; Chen, C. H.; Cheong, S. W. Percolative Phase Separation Underlies Colossal Magnetoresistance in Mixed-Valent Manganites. *Nature* **1999**, *399*, 560−563.

(8) Eerenstein, W.; Palstra, T. T. M.; Saxena, S. S.; Hibma, T. Spin-Polarized Transport across Sharp Antiferromagnetic Boundaries. *Phys. Rev. Lett.* **2002**, *88*, 247204.

(9) Venkateshvaran, D.; Althammer, M.; Nielsen, A.; Geprags, S.; Rao, M. S. R.; Goennenwein, S. T. B.; Opel, M.; Gross, R. Epitaxial $Zn_xFe_{3-x}O_4$ Thin Films: A Spintronic Material with Tunable Electrical and Magnetic Properties. *Phys. Rev. B: Condens. Matter Mater. Phys.* **2009**, *79*, 134405.

(10) Tripathy, D.; Adeyeye, A. O.; Boothroyd, C. B.; Piramanayagam, S. N. Magnetic and Transport Properties of Co-doped Fe_3O_4 Films. *J. Appl. Phys.* **2007**, *101*, 013904.

(11) Margulies, D. T.; Parker, F. T.; Rudee, M. L.; Spada, F. E.; Chapman, J. N.; Aitchison, P. R.; Berkowitz, A. E. Origin of the Anomalous Magnetic Behaviour in Single Crystal Fe_3O_4 Films. *Phys. Rev. Lett.* **1997**, *79*, 5162−5165.

(12) McKenna, K. P.; Hofer, F.; Gilks, D.; Lazarov, V. K.; Chen, C. L.; Wang, Z. C.; Ikuhara, Y. Atomic-Scale Structure and Properties of Highly Stable Antiphase Boundary Defects in Fe_3O_4. *Nat. Commun.* **2014**, *5*, 5740.

(13) Luders, U.; Barthelemy, A.; Bibes, M.; Bouzehouane, K.; Fusil, S.; Jacquet, E.; Contour, J. P.; Bobo, J. F.; Fontcuberta, J.; Fert, A. $NiFe_2O_4$: A Versatile Spinel Material Brings New Opportunities for Spintronics. *Adv. Mater.* **2006**, *18*, 1733−1736.

(14) Dhakal, T.; Mukherjee, D.; Hyde, R.; Mukherjee, P.; Phan, M. H.; Srikanth, H.; Witanachchi, S. Magnetic Anisotropy and Field Switching in Cobalt Ferrite Thin Films Deposited by Pulsed Laser Ablation. *J. Appl. Phys.* **2010**, *107*, 053914.

(15) Arora, S. K.; Wu, H. C.; Choudhary, R. J.; Shvets, I. V.; Mryasov, O. N.; Yao, H. Z.; Ching, W. Y. Giant Magnetic Moment in Epitaxial

DOI: 10.1021/acsnano.7b01743
ACS Nano 2017, 11, 5011−5019

Fe_3O_4 Thin Films on MgO(100). *Phys. Rev. B: Condens. Matter Mater. Phys.* **2008**, *77*, 134443.
(16) Silwal, P.; Miao, L.; Stern, I.; Zhou, X. L.; Hu, J.; Kim, D. H. Metal Insulator Transition with Ferrimagnetic Order in Epitaxial Thin Films of Spinel $NiCo_2O_4$. *Appl. Phys. Lett.* **2012**, *100*, 032102.
(17) Silwal, P.; Miao, L. D.; Hu, J.; Spinu, L.; Kim, D. H.; Talbayev, D. Thickness Dependent Structural, Magnetic, and Electronic Properties of the Epitaxial Films of Transparent Conducting Oxide $NiCo_2O_4$. *J. Appl. Phys.* **2013**, *114*, 103704.
(18) Bitla, Y.; Chin, Y. Y.; Lin, J. C.; Van, C. N.; Liu, R. R.; Zhu, Y. M.; Liu, H. J.; Zhan, Q.; Lin, H. J.; Chen, C. T.; Chu, Y. H.; He, Q. Origin of Metallic Behavior in $NiCo_2O_4$ Ferrimagnet. *Sci. Rep.* **2015**, *5*, 15201.
(19) Li, J. F.; Xiong, S. L.; Liu, Y. R.; Ju, Z. C.; Qian, Y. T. High Electrochemical Performance of Monodisperse $NiCo_2O_4$ Mesoporous Microspheres as an Anode Material for Li-Ion Batteries. *ACS Appl. Mater. Interfaces* **2013**, *5*, 981−988.
(20) Alcantara, R.; Jaraba, M.; Lavela, P.; Tirado, J. L. $NiCo_2O_4$ spinel: First Report on a Transition Metal Oxide for the Negative Electrode of Sodium-Ion Batteries. *Chem. Mater.* **2002**, *14*, 2847−2848.
(21) Zhang, G. Q.; Wu, H. B.; Hoster, H. E.; Chan-Park, M. B.; Lou, X. W. Single-Crystalline $NiCo_2O_4$ Nanoneedle Arrays Grown on Conductive Substrates as Binder-Free Electrodes for High-Performance Supercapacitors. *Energy Environ. Sci.* **2012**, *5*, 9453−9456.
(22) Cui, B.; Lin, H.; Li, J. B.; Li, X.; Yang, J.; Tao, J. Core-Ring Structured $NiCo_2O_4$ Nanoplatelets: Synthesis, Characterization, and Electrocatalytic Applications. *Adv. Funct. Mater.* **2008**, *18*, 1440−1447.
(23) Hu, L. F.; Wu, L. M.; Liao, M. Y.; Hu, X. H.; Fang, X. S. Electrical Transport Properties of Large, Individual $NiCo_2O_4$ Nanoplates. *Adv. Funct. Mater.* **2012**, *22*, 998−1004.
(24) Hu, L. F.; Wu, L. M.; Liao, M. Y.; Fang, X. S. High-Performance $NiCo_2O_4$ Nanofilm Photodetectors Fabricated by an Interfacial Self-Assembly Strategy. *Adv. Mater.* **2011**, *23*, 1988−1992.
(25) Coey, J. M. D.; Berkowitz, A. E.; Balcells, L.; Putris, F. F.; Barry, A. Magnetoresistance of Chromium Dioxide Powder Compacts. *Phys. Rev. Lett.* **1998**, *80*, 3815−3818.
(26) Sheng, P.; Abeles, B.; Arie, Y. Hopping Conductivity in Granular Metals. *Phys. Rev. Lett.* **1973**, *31*, 44−47.
(27) Knop, O.; Reid, K. I. G.; Sutarno; Nakagawa, Y. Chalkogenides of Transition Elements VI X-Ray Neutron and Magnetic Investigation of Spinels Co_3O_4 $NiCo_2O_4$ Co_3S_4 and $NiCo_2S_4$. *Can. J. Chem.* **1968**, *46*, 3463−3476.
(28) Xie, S.; Cheng, J.; Wessels, B. W.; Dravid, V. P. Interfacial Structure and Chemistry of Epitaxial $CoFe_2O_4$ Thin Films on $SrTiO_3$ and MgO Substrates. *Appl. Phys. Lett.* **2008**, *93*, 181901.
(29) Silwal, P.; Miao, L.; Hu, J.; Spinu, L.; Kim, D. H.; Talbayev, D. Thickness Dependent Structural, Magnetic, and Electronic Properties of the Epitaxial Films of Transparent Conducting Oxide $NiCo_2O_4$. *J. Appl. Phys.* **2013**, *114*, 103704.
(30) Xiao, J. Q.; Jiang, J. S.; Chien, C. L. Giant Magnetoresistance in Nonmultilayer Magnetic Systems. *Phys. Rev. Lett.* **1992**, *68*, 3749−3752.
(31) Xiong, P.; Xiao, G.; Wang, J. Q.; Xiao, J. Q.; Jiang, J. S.; Chien, C. L. Extraordinary Hall-Effect and Giant Magnetoresistance in the Granular Co-Ag System. *Phys. Rev. Lett.* **1992**, *69*, 3220−3223.
(32) Yakushiji, K.; Mitani, S.; Takanashi, K.; Ha, J. G.; Fujimori, H. Composition Dependence of Particle Size Distribution and Giant Magnetoresistance in Co−Al−O Granular Films. *J. Magn. Magn. Mater.* **2000**, *212*, 75−81.
(33) Helman, J. S.; Abeles, B. Tunneling of Spin-Polarized Electrons and Magnetoresistance in Granular Ni Films. *Phys. Rev. Lett.* **1976**, *37*, 1429−1432.
(34) Inoue, J.; Maekawa, S. Theory of Tunneling Magnetoresistance in Granular Magnetic Films. *Phys. Rev. B: Condens. Matter Mater. Phys.* **1996**, *53*, 11927−11929.
(35) Nagahama, T.; Santos, T. S.; Moodera, J. S. Enhanced Magnetotransport at High Bias in Quasimagnetic Tunnel Junctions with EuS Spin-Filter Barriers. *Phys. Rev. Lett.* **2007**, *99*, 016602.
(36) Muller, M.; Miao, G. X.; Moodera, J. S. Exchange Splitting and Bias-Dependent Transport in EuO Spin Filter Tunnel Barriers. *EPL* **2009**, *88*, 47006.
(37) Li, P.; Xia, C.; Zhu, Z. Y.; Wen, Y.; Zhang, Q.; Alshareef, H. N.; Zhang, X. X. Ultrathin Epitaxial Ferromagnetic γ-Fe_2O_3 Layer as High Efficiency Spin Filtering Materials for Spintronics Device Based on Semiconductors. *Adv. Funct. Mater.* **2016**, *26*, 5679−5689.
(38) Ziese, M.; Kohler, U.; Bollero, A.; Hohne, R.; Esquinazi, P. Schottky Barrier and Spin Polarization at the Fe_3O_4-Nb:$SrTiO_3$ Interface. *Phys. Rev. B: Condens. Matter Mater. Phys.* **2005**, *71*, 180406R.
(39) Brinkman, W. F.; Dynes, R. C.; Rowell, J. M. Tunneling Conductance of Asymmetrical Barriers. *J. Appl. Phys.* **1970**, *41*, 1915−1921.
(40) Moodera, J. S.; Hao, X.; Gibson, G. A.; Meservey, R. Electron-Spin Polarization in Tunnel-Junctions in Zero Applied Field with Ferromagnetic Eus Barriers. *Phys. Rev. Lett.* **1988**, *61*, 637−640.
(41) Moodera, J. S.; Santos, T. S.; Nagahama, T. The Phenomena of Spin-Filter Tunnelling. *J. Phys.: Condens. Matter* **2007**, *19*, 165202.
(42) Bergman, D. J.; Stroud, D. Physical Properties of Macroscopically Inhomogeneous Media. *Solid State Phys.* **1992**, *46*, 147−269.

DOI: 10.1021/acsnano.7b01743
ACS Nano 2017, 11, 5011−5019